AIAA SciTech Forum
8-12 January 2024, Orlando, FL
AIAA SCITECH 2024 Forum

10.2514/6.2024-1979

Millimeter-Wave Tomographic Interferometry of Ejecta Concentrations in Plume-Surface Interactions

Nicolas Rasmont[1], Ishaan Bansal[2], Hussein T. Al-Rashdan[3], Gregory S. Elliott[4], Joshua L. Rovey[5], and Laura Villafañe[6]
University of Illinois at Urbana-Champaign, Urbana IL, 61801

This study explores the ejecta dynamics of Plume-Surface Interactions (PSI). Utilizing radar tomography, a pioneering technique, we achieved the first quantitative mapping of ejecta concentrations in PSI experiments, overcoming the limitations of conventional optical methods hindered by the opacity of ejecta clouds. Our experimental setup is a Mach 5 jet impinging on a bed of regolith within a vacuum chamber, simulating planetary landing scenarios. We explored the impact of jet expansion on PSI phenomenology across different ambient pressure levels. In moderate underexpansion ($P_e/P_{amb} = 2.85 \rightarrow 2.45$) an initial surge in ejecta was followed by a steady-state phase, whereas high underexpansion ($P_e/P_{amb} = 338 \rightarrow 13.6$) conditions showed a gradual increase in ejecta concentration near the nozzle. Post-test crater analyses further underscored these differences, suggesting diverse erosion mechanisms. The moderate underexpansion condition yielded craters with sunken ridges and gentle slopes (15.6°), likely formed by the collapse of a deep transient crater. In contrast, high underexpansion resulted in craters with raised ridges and steep slopes (21.8°), indicative of viscous erosion.

I. Nomenclature

A	=	Forward Abel transform matrix
a_e	=	Speed of sound at nozzle exit
α	=	Regularization parameter in tomographic reconstruction
AoA	=	Angle of Arrival
b	=	Path-integrated measurements vector in tomographic reconstruction
β	=	Soil strength parameter
β_n	=	Slope of the radar interferometer calibration curve
BPM	=	Binary Phase Modulation
D_5, D_{50}, D_{95}	=	Particle diameter at 5th, 50th, and 95th percentile
D_c	=	Crater diameter
D_e	=	Exit diameter of the nozzle
$\bar{D}_p$	=	Average particle diameter
δ_p	=	Particle volume fraction
$\Delta\phi$	=	Measured phase shift
$\Delta\rho$	=	Gas-particle density difference
d_{N2}	=	Molecular diameter of nitrogen
FMCW	=	Frequency-Modulated Continuous-Wave
Fr_d	=	Densimetric Froude number
γ	=	Heat capacity ratio
h_c	=	Crater depth
h_e	=	Nozzle exit height above the surface
h_r	=	Reconstruction plane height above surface
h_{rim}	=	Rim height above surface

[1]PhD Candidate, Department of Aerospace Engineering, 324 Talbot Laboratory, 104 South Wright St, AIAA Student member.
[2]Undergraduate Student, Department of Aerospace Engineering, 324 Talbot Laboratory, 104 South Wright St.
[3]PhD Candidate, Department of Aerospace Engineering, 324 Talbot Laboratory, 104 South Wright St, AIAA Student Member.
[4]Professor, Department of Aerospace Engineering, 301 Talbot Laboratory, 104 South Wright St, AIAA Associate Fellow.
[5]Professor, Department of Aerospace Engineering, 317 Talbot Laboratory, 104 South Wright St, AIAA Associate Fellow.
[6]Assistant Professor, Department of Aerospace Engineering, 313 Talbot Laboratory, 104 South Wright St, AIAA Senior Member.

K	=	Hypersonic similarity parameter
k_B	=	Boltzmann constant
Kn_p	=	Knudsen number for particles
L_{fd}	=	Finite difference matrix in tomographic reconstruction
$L_{\sigma_D}(x, y)$	=	Laplacian of Gaussian map of crater
$\dot{m}$	=	Mass flow rate of the jet
M_e	=	Mach number at nozzle exit
MIMO	=	Multiple-In Multiple-Out
μ_e	=	Dynamic viscosity at nozzle exit
n_p	=	Particle number concentration
p_{amb}	=	Initial ambient pressure
p_e	=	Static pressure at nozzle exit
PLA	=	Polylactic Acid
PSI	=	Plume-Surface Interactions
ψ_c	=	Crater slope
PTFE	=	Polytetrafluoroethylene
Re_n	=	Nozzle Reynolds number
Re_p	=	Particle Reynolds number
ρ	=	Fluid density
ρ_{bulk}	=	Bulk density of particles
ρ_e	=	Fluid density at nozzle exit
σ	=	Normal stress
σ_D	=	Standard Deviation of Gaussian Filter
T_e	=	Temperature at nozzle exit
θ	=	Angle of repose
u_e	=	Velocity at nozzle exit
V_c	=	Crater volume
$\bar{x}$	=	Reconstructed ejecta values in tomographic reconstruction

II. Introduction

PLUME-surface interactions (PSI) refer to the set of complex physical phenomena caused by the impingement of an exhaust plume on a granular surface, typical of a powered planetary landing. PSI are the cause of several hazards for landing spacecrafts, including the formation of an opaque cloud of ejecta capable of blinding guidance systems, a deep crater capable of burying or toppling the spacecraft, and supersonic ejecta, which can sandblast the spacecraft and any nearby infrastructure[1–5]. Within the context of the the Artemis Program's return of human missions to the Moon, those hazards must be well-understood and mitigated to allow for safe future landings. The Starship Human Landing System is two orders of magnitude larger and heavier than the Apollo Lunar Module, with correspondingly more severe PSI hazards. PSI are challenging for experimental study because of the opacity of the ejecta cloud, which limits the usefulness of conventional optical diagnostics for ejecta and cratering measurements [6, 7]. For ground-based experiments, the most common mitigation technique involves a transparent splitter plate, which provides optical access to the center of the crater [1–3, 8–12]. Although it allows real-time observation of the crater formation, this technique is invasive, as it introduces a disturbance directly in the jet.

Our research is focused on the development and use of non-invasive diagnostic techniques to measure the concentration of the ejecta cloud. We use a Mach 5 jet impinging on a bed of regolith in a vacuum chamber as a reduced-scale PSI experiment. By varying the pressure in the chamber, and thus the jet expansion ratio, we can replicate some of the non-dimensional flow and erosion parameters characteristic of Lunar and Martian landings. The concentration of ejecta is mapped using millimeter-wave radar tomographic interferometry, a novel measurement technique we developed that is capable of measuring the concentration of an optically opaque cloud of airbone particles non-intrusively and at a high temporal resolution (10 kHz). Prior works by the authors [13, 14] demonstrated the capabilities of millimeter-wave interferometry to measure path-integrated ejecta concentration and its potential for tomographic measurements. For the first time, we present quantitative measurements of ejecta concentration in a PSI experiment. Concurrent high-speed imaging and 3D scanning of the post-test crater surface provide further information about PSI physics.

III. Methods

A. Plume-Surface Interaction Experiment

The Plume-Surface Interaction facility used in this study has been described in previous works [13–15]. It consists of a cold Mach 5 nitrogen jet impinging on a bed of regolith simulant. The jet is generated by a bell nozzle with an exit diameter of 1 cm and an expansion ratio of 25. The nozzle is mounted on a vertical linear stage with a travel of 15cm, in a normal orientation to the granular surface. The nozzle and granular bed shown in Fig. 1 are located in a 2375 L vacuum chamber equipped with a 60 cm acrylic window providing optical access. A 38 L (10 gal) tank located above the chamber and kept at ambient temperature feeds nitrogen to the nozzle through a solenoid valve. The mass flow rate is regulated by varying the static pressure within the tank.

Fig. 1 Photograph of the PSI apparatus through the large-diameter window showing the cold gas nozzle (1), granular media bed (2), radar (3), and reflectors (4). ***(Note: Rectangular reflectors were used during data collection instead of the circular reflectors shown here, see Fig. 3.)***

During the experiment, the jet is pulsed for a duration of 1 second to clear the 18ms initial jet transient and limit the increase in ambient pressure due to the injected gas to 125 Pa at jet cutoff. Monodisperse glass microspheres with a 109 μm mean diameter were selected as a regolith simulant. Particle size distribution percentiles and other relevant properties, such as the angle of repose, bulk density and solid volume fraction are given in Table 1. The parameters varied in the experiment are the height of the nozzle exit plane above the surface h_e/D_e, the initial ambient pressure P_{amb}, and the jet mass flow rate $\dot{m}$. Each of those parameters can take a low and a high value for a total of 8 distinct combinations shown in Fig 2. In this paper, we report results for two combinations: high flow rate, high altitude, high ambient pressure and high flow rate, high altitude, low ambient pressure.

Table 1 Properties of the glass microspheres used as regolith simulant, with size distribution from [14].

Parameter	Value
$\bar{D}_p$ (μm)	109
D_5 (μm)	79
D_{50} (μm)	108
D_{95} (μm)	142
θ (°)	24
δ_p (%)	59
ρ_{bulk} ($kg.m^{-3}$)	1470

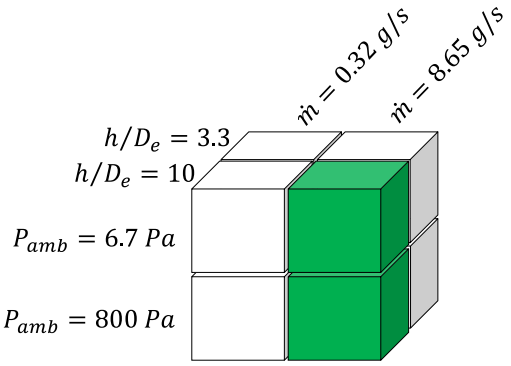

Fig. 2 Parameter space of tested conditions. Highlighted in green are the two combination of parameters for which results are reported.

A set of non-dimensional flow parameters relevant to PSI physics is presented in Table 2 for the current experiment at low pressure and high flow rate. Jet flow physics are matched to a a nominal full-scale human lunar lander by reproducing the Mach number M_e, hypersonic similarity parameter K, nozzle Reynolds number Re_p, densimetric Froude number Fr_d and heat capacity ratio γ. The exit pressure ratio P_e/P_{amb} decreases during experiment due to the increase in ambient pressure. Nevertheless, the jet remains highly underexpanded ($P_e/P_{amb} \gg 4$), which results in a similar flow structure despite the jet contraction, with a standing plate shock above the surface and surface pressures unchanged near the stagnation point[15, 16]. For the high pressure case, the decrease in P_e/P_{amb} over the experiment is not significant enough ($2.85 \rightarrow 2.45$) to have a large impact on PSI physics.

Table 2 Non-dimensional flow parameters for the current experiment operating at $\dot{m}$=8.6 g/s and P_{amb} = 6.7 Pa and whether they are matched to a nominal full-scale human lunar lander.

Dimensionless Parameter	Parameter Equation	Reduced-Scale (Current Experiment)	Matched/ Unmatched
Mach	$M_e = u_e/a_e$	5	✓
K	$K = \gamma(\gamma-1)M_e^2$	14	✓
P_e/P_{amb}	-	338 ($t = 0\ s$) $\rightarrow$ 13.6 ($t = 1\ s$)	✓
γ	-	1.4	✓
Re_n	$Re_n = \rho_e u_e D_e/\mu_e$	3.6×10^5	✓
Re_p	$Re_p = (\rho_e u_e \bar{D})/[\mu_e(1-n)]$	8530	×
Fr_d	$Fr_d = u_e/(g\bar{D}\Delta\rho/\rho)^{0.5}$	171.5	✓
Kn_p	$Kn_p = k_B T_e/(\pi P_e d_{N2}\bar{D}/\sqrt{2})$	$< 10^{-2}$	×
β	$\beta = (c + \sigma\tan\theta)/p$	0.46	×

Not all non-dimensional parameters representative of flow, erosion and granular physics can be simultaneously reproduced on a sub-scale ground experiment [8, 17]. The high flow rate used in the experiment allows the non-dimensional parameters most relevant to surface forces ($Re_n, M_e, Fr_d, \gamma, P_e/P_{amb}$) to be matched with the full-scale case. However, the combination of low jet temperature (< 50 K) and large particle size leads to a much lower Knudsen number Kn_p in the experiment than at full-scale, which means that rarefaction effects will not be accurately captured. The particle Reynolds number Re_p is much larger in the experiment for the same reasons. Kn_p and Re_p are more closely matched to the full-scale case in low mass flow rate experiments ($\dot{m} = 0.032\ g.s^{-1}$). In addition, non-cohesive monodisperse glass microspheres are a significant simplification over the broad particle size distributions and highly cohesive nature of Lunar and Martian soils [18–20], resulting in a lower soil strength β. This simplification was adopted to allow comparison with numerical models of PSI, which usually assume spherical particles, as well as to facilitate further analysis and interpretation of results.

B. Tomographic mmWave Radar Instrument

The tomographic mmWave radar instrument used in this study is an upgraded version of a mmWave radar interferometer, whose operating principle, preliminary results, and calibration procedure have been described in previous works [13, 14, 21]. It consists of a Texas Instrument IWR1443 frequency-modulated continuous-wave (FMCW) radar illuminating an array of 7 plate reflectors. The radar chirps at frequencies between 77 and 81 GHz at a repetition rate of 10 kHz. The radar is enclosed in a Polylactic acid (PLA) and Polytetrafluoroethylene (PTFE) enclosure which shields it from ejecta impact. A custom-made PTFE lens focuses the radar beam in the vertical direction to minimize secondary reflections on the granular surface. The reflectors are aluminum plates with a height of 31.75 mm and a width inversely proportional to the square of the radar-reflector distance in order to equalize the amplitudes of the reflector peaks. The array is mounted on height-adjustable posts made of acrylic and PLA and covered in mmWave-absorptive foam to reduce non-reflector clutter and secondary reflections. The phase of the signal reflected by each reflector provides the value of the particle number concentration integrated along the radar-reflector propagation path, according to equation 1:

$$\Delta\phi = \beta_n \int_{\text{Radar}}^{\text{Reflector}} n_p dl \tag{1}$$

With $\Delta\phi$ the phase shift of the signal compared to an unladen propagation path, β_n the calibration constant of the instrument for the ejecta material, and n_p the local number concentration of particles. The calibration constant was measured to be $\beta_n = (1.379 \pm 0.043) \times 10^{-7}$ °.#$^{-1}$.m^2 in [14]. A picture of the reflector array is shown in Fig. 3(a) alongside the corresponding signal measured by the radar shown in Fig. 3(b). The radar signal is presented as a range-azimuth map: the color of each pixel represent the amplitude of the echo measured by the radar at a specific azimuth angle-of-arrival (AoA) and range bin. The ability to resolve the AoA of incoming signals is implemented using Multiple-In Multiple-Out (MIMO) binary phase modulation (BPM) [22] on the transmit antennas. AoA resolution is a significant improvement over the previous iteration of the interferometer, which could only measure range, as it allows more effective clutter rejection and better isolation between reflectors. The peaks corresponding to each reflector are clearly identifiable in Fig. 3(b).

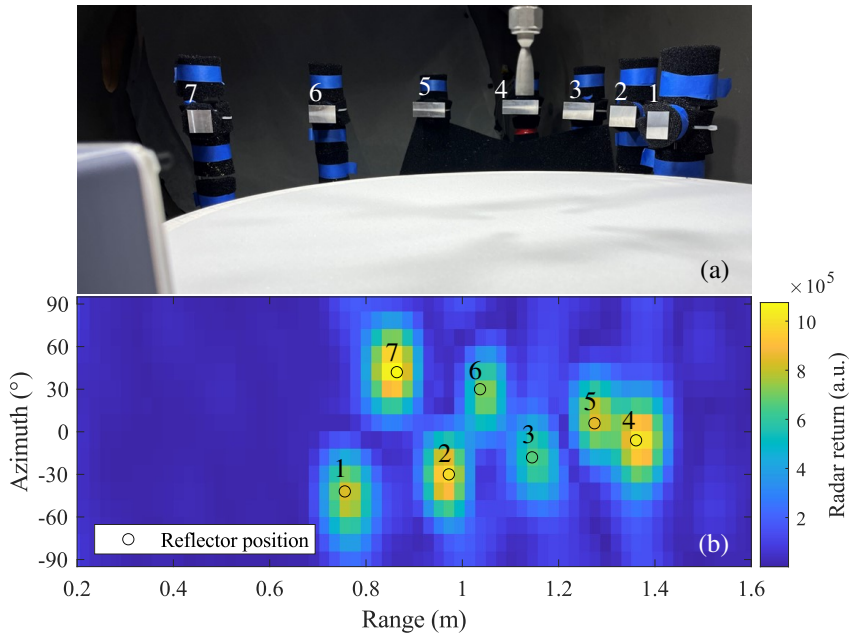

Fig. 3 Reflector array (a), and corresponding range-azimuth map measured by the radar (b).

The instrument's path-integrated measurements do not inherently reveal the spatial distributions of ejecta. To address this, we have implemented a tomographic technique for reconstructing local ejecta concentrations. This technique, based on multiple path-integrated measurements from reflectors, assumes an axisymmetric particle concentration distribution around the jet axis, justified by the normal orientation of the nozzle relative to the surface. The axisymmetric assumption permits the use of an Abel transform-based reconstruction technique[23, 24] to derive local concentrations from a

sparse set of path-integrated measurements.The configuration of the reflector array used in our study is depicted in Fig. 4. The array defines a surface-parallel slice for reconstructing local concentrations within seven concentric regions. We optimized the spatial arrangement of the array to maximize the angular and range separation between consecutive reflectors, enhancing signal isolation in radar data.

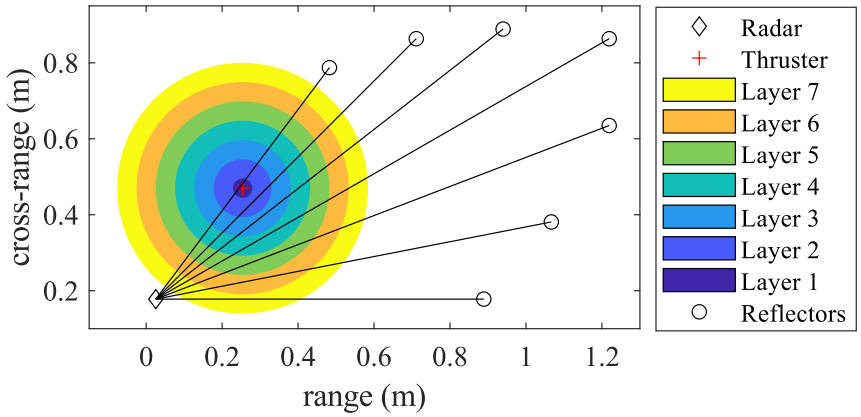

Fig. 4 Locations of the path-integrated measurements arms and inverse Abel reconstruction regions.

The path-integrated measurements are converted to local concentrations using a Tikhonov regularization of the onion-peeling algorithm first described by Daun [25], and implemented via the PyAbel Python package [26]. A non-negativity condition within this technique prevents the generation of nonphysical negative concentrations, a potential issue in noisy data scenarios. The overall equation of the Abel transform is given in Eq. 2, with $\bar{x}$ the reconstructed ejecta values, A the forward Abel transform matrix for the chosen basis set (in our case, piecewise quadratic), b the path-integrated measurements, α a regularization parameter and L_{fd} the finite difference matrix.

$$\bar{x} = \arg\min_{x} \left(\|Ax - b\|^2 + \alpha \|L_{\text{fd}} x\|^2 \right) \tag{2}$$

A preliminary 3-reflector setup described in prior work by the authors[14] served as a proof of concept. While it was a significant step forward, the conventional onion-peeling tomographic reconstruction technique used then was very sensitive to measurement noise, and the limited reconstruction area restricted the utility of the measurements. In contrast, the current experimental setup with a 7 reflector array, coupled with an enhanced reconstruction technique, overcomes these limitations to produce high-quality data. The details and results of this improved approach are discussed in Sections IV.A and IV.B. For each set of experimental conditions, the concentration of particles was mapped in two slices located at different heights above the surface: $h_r/D_e = 3$ and $h_r/D_e = 6$, in red and blue respectively in Fig. 5.

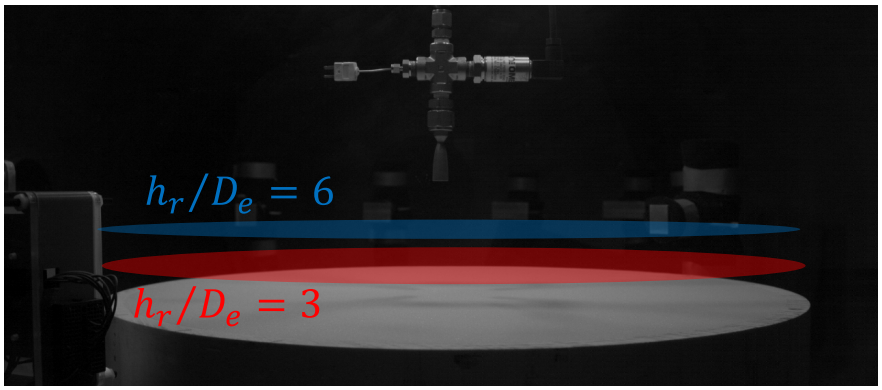

Fig. 5 Location of the measurement planes probed by the instrument above the granular surface.

C. Post-test Crater Measurements

Evaluating how the properties of the crater vary with experimental conditions can provide additional insight into PSI physics and provide an independent validation of ejecta measurements. To do this, we measured the depth, diameter, volume and cross-section of the post-experiment crater. The measurement pipeline is presented in Fig. 6 and consists of:

- First, we use Azure Kinect 3D scanner in conjunction with the RecFusion software to scan the granular surface (Fig. 6(a)), generating a triangular mesh of the crater with a resolution of 0.3 mm;
- The mesh is then converted to a topographic map of the form $z = S(x, y)$ (Fig. 6(b));
- The depth of the crater is calculated by measuring the vertical distance between the lowest point on the map and the undisturbed surface;
- We calculate the crater boundary (Fig. 6(c)) and perform a least-square circle fit, which provides the crater diameter. Further detail on the crate boundary calculation will be given below;
- Finally, we measure the volume of the crater under the undisturbed surface (Fig. 6(d)). We generate a closed mesh of the crater by intersecting the crater mesh with a plane coplanar with the undisturbed surface. The volume of this closed mesh is then calculated using a signed sum-of-tetrahedra.
- Crater cross-sections are generated using ray-tracing, by measuring the position of mesh intersections with an array of upward-pointing rays aligned with a diameter of the crater.

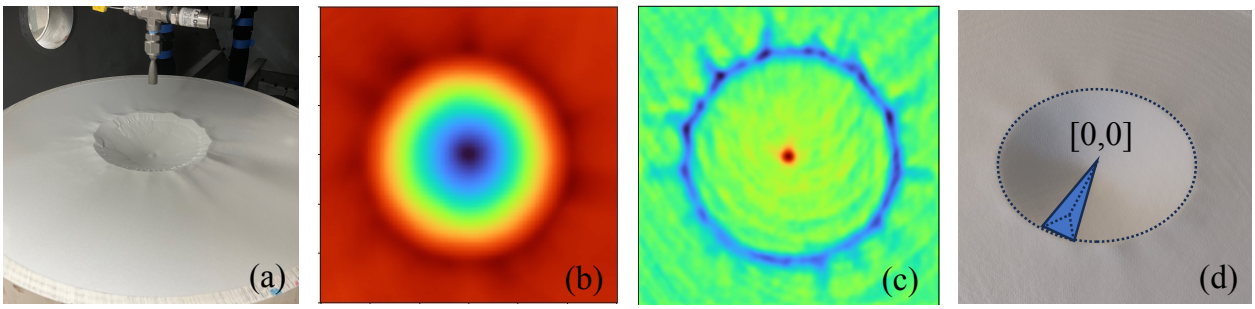

Fig. 6 Intermediary steps of the post-test crater measurement procedure: physical crater (a), elevation map (b), crater edge (c), sum-of-tetrahedra volume measurement (d).

There exist multiple definitions of crater boundaries which are not consistent across researchers and disciplines. Turtle et al. [27] identifies 7 definitions of diameter in planetary impact craters; Stubbs et al. [28] use the elevation contour located 5 mm below the undisturbed surface as the boundary in their PSI craters; Balakrishnan and Bellan [29] define the crater boundary as the region of maximum volume fraction in the bulk granular materials. The most commonly used crater edge definition uses the maximum rim height, which is undefined in craters with sunken rim.

In this work, we introduce a novel definition of the crater boundary as the region of minimum Laplacian around the impingement point. This definition aims at capturing the abrupt change in slope between the flat undisturbed surface and the crater itself. The key benefit of this definition is that it is based on surface topography exclusively,is independent of the crater scale, and is not affected by a sunken or raised ridge. However, it can be disturbed by small-scale crater features such as terraces or scanning artifacts such as Moiré patterns. Consequently, we use a Gaussian low-pass spatial filter to remove those features before applying the Laplacian operator to the surface. The Laplacian of Gaussian (LoG) is a commonly used edge detection algorithm in image processing [30–32]. The overall equation of the LoG filter is provided in Eq. 3 with $S(x, y)$ the input tomographic height map and $L_{\sigma_D}(x, y)$ the filtered surface for a Gaussian standard deviation σ_D. After the filter has been applied, the maximum of the LoG map is measured along a set of radial cross-sections around the impingement point. The resulting set of points constitute the crater boundary.

$$L_{\sigma_D}(x, y) = \sigma_D^2 \Delta \left[\int_{\tau_1=-\infty}^{+\infty} \int_{\tau_2=-\infty}^{+\infty} S(x, y) \exp\left(\frac{-1}{\sigma_D^2} \left((x - \tau_1)^2 + (y - \tau_2)^2 \right) \right) d\tau_1 d\tau_2 \right] \tag{3}$$

IV. Results

In this section, we present the results of ejecta radar tomography and post-experiment crater measurements acquired for the two experimental conditions described in Fig. 2, referred to as moderate underexpansion (P_{amb} = 800 Pa) and

high underexpansion (P_{amb} = 6.7 Pa). To the authors' knowledge, it is the first reported quantitative measurement of ejecta concentrations in a PSI experiment.

A. Moderate underexpansion ejecta

The ejecta concentrations measured by the interferometer in the moderate-underexpansion case are presented in Fig. 7(a) and (b) for the two tested heights above the surface, h_r/D_e = 3 and h_r/D_e = 6 respectively. The concentration is depicted on a color map, where the y-axis represents the distance to the nozzle, and the x-axis denotes time. The color intensity follows a logarithmic scale correlating with the particle number concentration (#.m^{-3}), with a minimum threshold at 10^8 #.m^{-3}. The reconstructed ejecta distribution is axisymmetric, allowing the concentration in the 2D slice probed by the instrument to be effectively summarized into a 1D vector at each measurement time. The boundaries of the tomographic reconstruction regions are indicated on the plot as solid white lines. The jet end time at t = 1 s is also plotted to provide temporal context. The concentration distributions in the two measurement planes show similar features. First, a large initial ejecta surge is apparent, which manifests as a very high-density region moving outward during the first 400 ms of the experiment. A snapshot from the high-speed camera recording of the surge is shown in Fig. 8(a). The optical opacity of the ejecta cloud is evident in these images. The maximum density measured during the surge is 3.75×10^{10} #.m^{-3} for h_r/D_e = 3 and 2.45×10^{10} #.m^{-3} for h_r/D_e = 6.

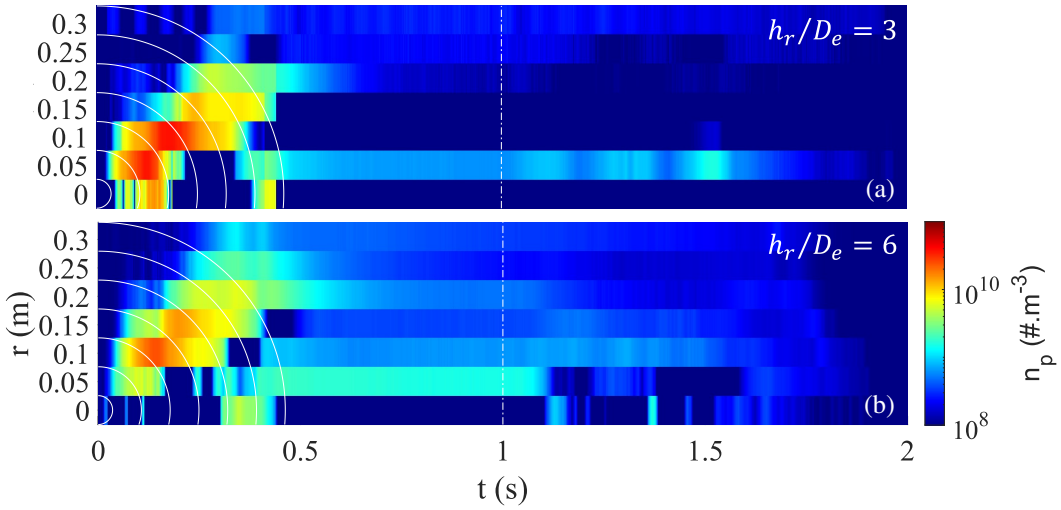

Fig. 7 Concentration of ejecta as a function of radial distance to the nozzle r and time for a measurement plane height h_r/D_e = 3 (a) and h_r/D_e = 6 (b) for a moderately underexpanded jet (h_e/D_e = 10, m = 8.6 g.s^{-1}, P_{amb} = 800Pa).

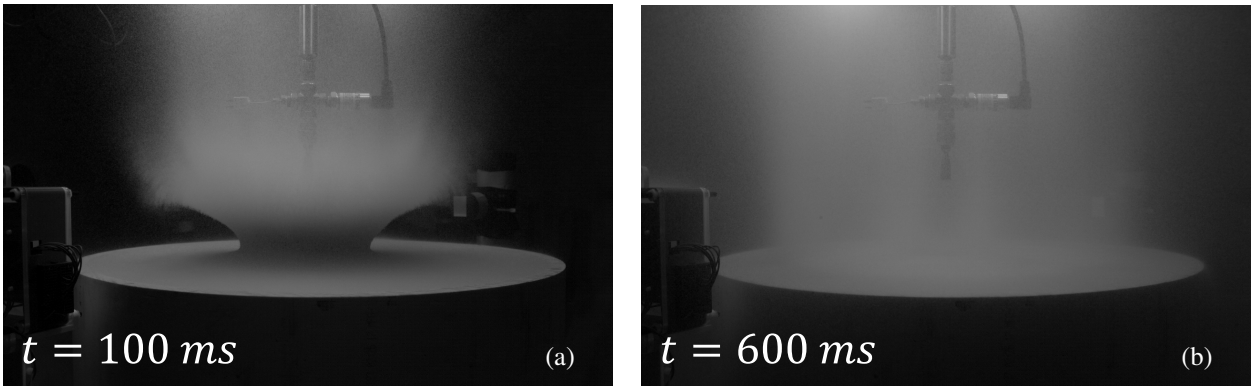

Fig. 8 High-speed images of ejecta in the moderate underexpansion experiment at t = 100 ms (a) (initial surge), and t = 600 ms (b) (steady state).

During the steady state regime (t > 400 ms), the measured ejecta concentration is one order of magnitude lower than in the surge. This is clearly visible in Fig. 8(b), in which the ejecta cloud is less opaque than in Fig. 8(a). The center bin (at r = 0 m) in Fig. 7 is completely empty, presumably due to the presence of the jet flushing particles down and preventing any lingering ejecta. In addition, the concentration at high altitude is 2.5 times higher than at low altitude. The radial distribution of ejecta at $h_r/D_e = 3$ presents a gap, with little particles detected in the r = 0.10 m and r = 0.15 m bins. The gap is less severe in the $h_r/D_e = 6$ measurement. We interpret those features as indication of particles following an arced near-ballistic trajectory: particles cannot reach low altitude mid-bands because their emission angle and initial velocity are too high. Those features are identical to those observed with the path-integrated centerline measurements presented in [14] at $h_r/D_e = 3$ and $h_r/D_e = 6$: high concentration at low altitude during the surge, high concentration at high altitude during the steady-state. The spatial resolution provided by the tomographic reconstruction further supports the observation that particles are emitted at a high angle from the surface and follow a near-ballistic arc during the steady-state regime.

B. High underexpansion ejecta

Ejecta tomography results for the high-underexpansion case are presented in Fig. 9 and corresponding high-speed images in Fig 10. The behavior of the ejecta is different from the moderate-underexpansion case. There is no surge nor steady-state regime: the ejecta concentration gradually increases over time and collimates toward the nozzle. The data from the two measurement planes shows the same broad trends, with the exception that concentrations at $h_r/D_e = 3$ are 54% higher than concentrations at $h_r/D_e = 6$ on average. The particle concentrations measured in the high underexpansion case are of the same order of magnitude as the moderate-underexpansion steady state ($\sim 10^9\ \#.m^{-3}$), eventually exceeding them as the jet collimates, with maximums of $5.28 \times 10^9\ \#.m^{-3}$ at $h_r/D_e = 3$ and $3.5 \times 10^9\ \#.m^{-3}$ at $h_r/D_e = 6$.

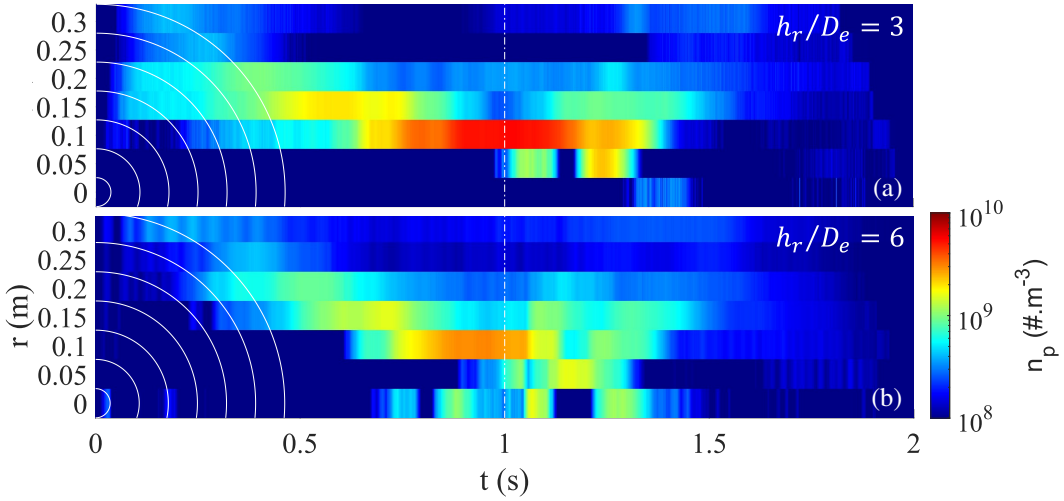

Fig. 9 Concentration of ejecta as a function of radial distance to the nozzle r and time for a measurement plane height $h_r/D_e = 3$ (a) and $h_r/D_e = 6$ (b) for a highly underexpanded jet ($h_e/D_e = 10, m = 8.6\ g.s^{-1}, P_{amb} = 6.7Pa$).

The high-speed footage provides further insight into the ejecta phenomenology. Over time, the cloud contracts through an increase in the emission angle of the ejecta from the crater, going from near-horizontal at the onset of the jet to near vertical at the cutoff, as in Fig. 10(a) and Fig. 10(b). A potential explanation is that as the crater forms, the surface slope increases. In the viscous erosion regime expected at high underexpansion, particles are sheared parallel to the surface: an increase in slope consequently results in a progressively higher ejecta angle over time. This could be compounded by the contraction of the plate shock over the surface as the ambient pressure increases. This behavior is fully in line with the trends previously observed in path-integrated measurements at similar expansion ratios in our previous works [13, 14]. The presence of streaks in the ejecta cloud during the latter part of the experiment is notable in Fig. 10(b). Other studies have also observed ejecta streaking in high-underexpansion jet impingements [10, 13].

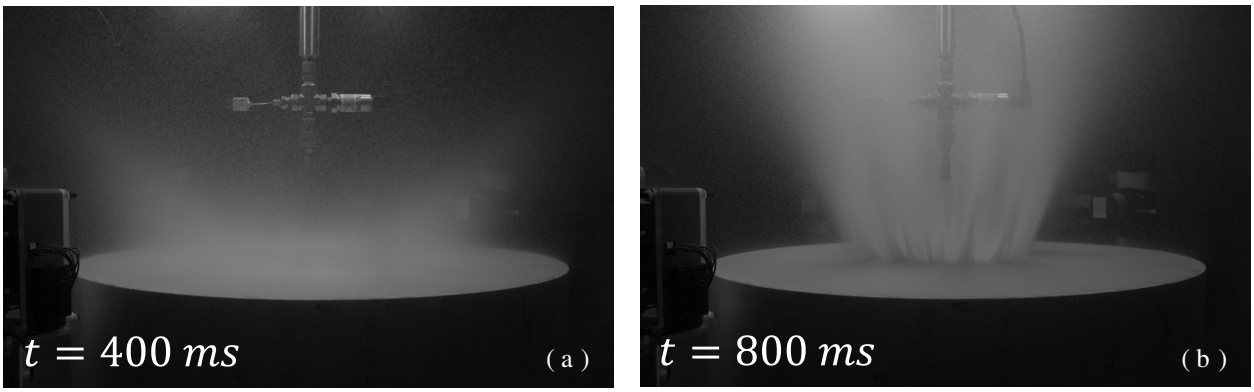

Fig. 10 High-speed images of ejecta in the high underexpansion experiment at t = 400 ms **(a) and** t = 800 ms **(b), showing streaks.**

C. Post-test Crater

The cross-sections of the high underexpansion and moderate underexpansion post-test crater geometries are presented in Fig. 11. The depth, diameter, ridge height and volume of the craters are reported in Table 3. The primary differences between the two crater cross-sections can be seen in the rim and slope. The highly underexpanded crater has a raised ridge, while the moderate underexpansion case has a 28% gentler slope and a sunken ridge. Notably, the moderate underexpansion crater, despite being 15% shallower, has a 24% greater width compared to the high underexpansion crater, leading to a 42% larger excavated volume.

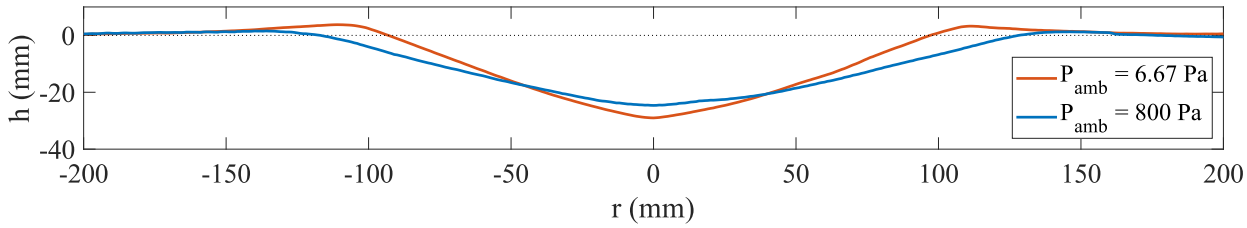

Fig. 11 Cross-section of the post-experiment craters in the high underexpansion and moderate underexpansion cases.

Table 3 Post-experiment crater properties for high underexpansion and moderate underexpansion cases.

Parameter	P_{amb} = 6.67 Pa	P_{amb} = 800 Pa
D_c (mm)	208 ± 2	257 ± 8
h_c (mm)	30 ± 0.7	25.4 ± 1.9
h_{rim} (mm)	+2.7 ± 0.2	−1.5 ± 2.7
V_c (L)	0.339 ± 0.007	0.483 ± 0.040
max ψ_c (°)	21.8 ± 2.0	15.6 ± 2.8

These differences are interpreted as indicators of distinct erosion mechanisms. Fig. 12 presents images taken in the half-space jet impingement experiment described by Rubio et al. [10] as illustrations of the different erosion mechanisms associated with PSI craters. For the moderate underexpansion scenario (Fig. 12(a)), the formation of the final crater is attributed to the collapse of a previously deeper crater, boring through the surface and leading to a shallower angle of repose. Conversely, in the high underexpansion case (Fig. 12(a)), the observed crater formation aligns with the process of viscous erosion described by Roberts [33], shearing particles parallel to the surface.

However, the highly underexpanded jet, as per Robert's theory, is expected to create a "donut" erosion pattern characterized by maximum erosion in an annular band while sparing the centerline. However, this distinctive pattern was not observed in our experiment. This deviation could be attributed to three main factors. Firstly, the central structure of the crater might collapse during the erosion process due to the granular material's low angle of repose reported in Table 1. Secondly, there might be a transition in the erosion mechanism from viscous shear erosion to another form, such as diffusion-driven erosion or bearing capacity failure. Such a shift could result in erosion being concentrated at the crater's center, wiping earlier viscous erosion features. This transition can be caused by the contraction of the jet, and the associated increase in ground pressure, as the ambient pressure increases during the experiment. Lastly, suspended particles falling back down to the surface after the end of the jet can alter the crater geometry, possibly obscuring viscous erosion features.

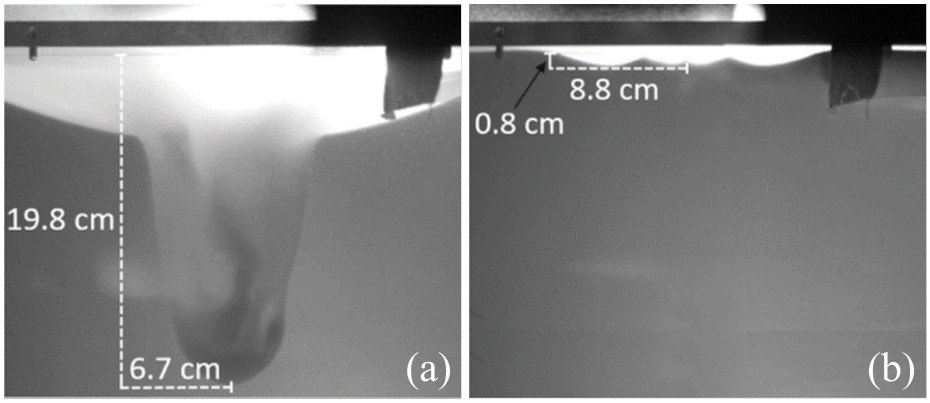

Fig. 12 Cross-section of the transient (i.e. with active jet) craters generated by moderate underexpansion (a) and high underexpansion (b) supersonic jet in glass microspheres reported by Rubio et al. [10].

V. Conclusion

This study has analyzed the dynamics of ejecta production in PSI experiments and the resultant crater formation under two jet underexpansion conditions: $P_e/P_{amb} = 338 \rightarrow 13.6$ (high underexpansion) and $P_e/P_{amb} = 2.85 \rightarrow 2.45$ (moderate underexpansion). Ejecta measurement were performed using radar tomography, a novel technique capable of measuring the concentration of optically opaque ejecta clouds at a high temporal resolution. High-speed imaging and post-test crater scanning complement the ejecta tomography. This diagnostic suite was used to study the underlying physics of cratering and ejecta dynamics. We presented maps of quantitative ejecta concentrations, which are the first of their kinds: to the authors' knowledge, ejecta concentrations have never been measured in a PSI experiment before.

Our results highlight differences in ejecta behavior and crater formation between high and moderate underexpansion scenarios. In the moderate underexpansion condition, we observed a pronounced initial surge in ejecta production followed by a steadier, more homogeneous phase, with one order of magnitude lower concentrations: $\sim 10^{10} \rightarrow 10^9$ #.m^{-3}. The high underexpansion condition exhibited a gradual increase in ejecta concentration with a more focused distribution around the nozzle, and maximum concentrations of 5.28×10^9 $\#.m^{-3}$. Those measurements are consistent with previous path-integrated measurements performed in similar conditions. The post-test crater measurements further reinforced these distinctions, revealing different erosion mechanisms at play. The moderate underexpansion condition produced a shallow, wide craters with sunken ridges, indicative that this crater was formed through the collapse of a deep transient crater. In contrast, the high underexpansion condition resulted in craters with raised ridges and 40% steeper slopes, aligning with a process of viscous erosion.

The techniques presented in this work are mature, and the detailed information they provides paves the way towards an improved understanding of PSI physics. Quantitative ejecta concentrations are a rich dataset: they can be used to evaluate surface erosion properties, through particle trajectory back-propagation as well as ejecta velocity and flux, which are all critical parameters for evaluating PSI risks during planetary landings.The quantitative crater and ejecta measurements presented here are valuable for the validation and calibration of numerical and theoretical models of PSI. The usefulness of radar tomography is not limited to PSI experiments; It can be readily applied to any opaque particle-laden gas flow, with possible areas of applications in meteorology, fire safety, and industrial powder handling.

VI. Acknowledgements

This work is supported by the National Aeronautics and Space Administration (NASA) under Grant No. 80NSSC20K0304 issued through the Early Stage Innovation Program and Grant No. 80NSSC22K1332 through the Future Investigator In NASA Earth and Space Science and Technology. We acknowledge the contributions of Dr. Danehy, NASA Research Collaborator, through fruitful comments and discussions, and Liam Heuser, undergraduate research assistant, for his contributions to the non-dimensional numbers calculations and analysis.

References

[1] Metzger, P. T., Immer, C. D., Donahue, C. M., Vu, B. T., Latta III, R. C., and Deyo-Svendsen, M., "Jet-induced cratering of a granular surface with application to lunar spaceports," *Journal of Aerospace Engineering*, Vol. 22, No. 1, 2009, pp. 24–32.

[2] Metzger, P., Li, X., Immer, C., and Lane, J., "ISRU Implications for Lunar and Martian Plume Effects," *47th AIAA Aerospace Sciences Meeting including The New Horizons Forum and Aerospace Exposition*, 2009. https://doi.org/10.2514/6.2009-1204, URL http://dx.doi.org/10.2514/6.2009-1204.

[3] Metzger, P. T., Latta, R. C., Schuler, J. M., and Immer, C. D., "Craters Formed in Granular Beds by Impinging Jets of Gas," *AIP Conference Proceedings*, Vol. 1145, No. 1, 2009, pp. 767–770. https://doi.org/10.1063/1.3180041, URL https://aip.scitation.org/doi/abs/10.1063/1.3180041.

[4] Wagner, S. A., "The Apollo experience lessons learned for constellation lunar dust management," *NASA Technical Publication TP-2006-213726. Washington, DC: National Aeronautics and Space Administration*, 2006.

[5] Immer, C., Metzger, P., Hintze, P. E., Nick, A., and Horan, R., "Apollo 12 Lunar Module exhaust plume impingement on Lunar Surveyor III," *Icarus*, Vol. 211, No. 2, 2011, pp. 1089–1102. https://doi.org/https://doi.org/10.1016/j.icarus.2010.11.013, URL https://www.sciencedirect.com/science/article/pii/S001910351000432X.

[6] Metzger, P. T., Dove, A., Conroy, M., Gloria, J., O'Reilly, A., and St. John, A., "Ejecta Sheet Tracking, Opacity, and Regolith Maturity (Ejecta Storm): An Instrument for Lunar Landing Plume Effects and Dust Dynamics," *Lunar and Planetary Science Conference*, 2021, p. 2616.

[7] Lane, J. E., Mantovani, J. G., Mueller, R. P., Nugent, M. W., Nick, A. J., Schuler, J. M., and Townsend, I. I., "Optical Extinction Measurements of Dust Density in the GMRO Regolith Test Bin," *Earth and Space 2016*, 2016, pp. 36–47. https://doi.org/10.1061/9780784479971.005, URL https://ascelibrary.org/doi/abs/10.1061/9780784479971.005.

[8] Korzun, A. M., Eberhart, C. J., West, J., Liever, P., Weaver, A., Mantovani, J., Langton, A., Kemmerer, B., and Atkins, A., "Design of a Subscale, Inert Gas Test for Plume-Surface Interactions in a Reduced Pressure Environment," *AIAA SCITECH 2022 Forum*, AIAA, 2022, p. 1808. https://doi.org/10.2514/6.2022-1808, URL https://arc.aiaa.org/doi/abs/10.2514/6.2022-1808.

[9] Diaz-Lopez, M. X., Gorman, M., Rubio, J. S., and Ni, R., "Plume-surface Interaction Physics Focused Ground Test 1: Diagnostics and Preliminary Results," *AIAA SCITECH 2022 Forum*, AIAA, 2022. https://doi.org/10.2514/6.2022-1810, URL https://arc.aiaa.org/doi/abs/10.2514/6.2022-1810.

[10] Rubio, J. S., Gorman, M., Diaz-Lopez, M. X., and Ni, R., "Plume-Surface Interaction Physics Focused Ground Test 1: Setup and Preliminary Results," *AIAA SCITECH 2022 Forum*, 2022. https://doi.org/10.2514/6.2022-1809, URL https://arc.aiaa.org/doi/abs/10.2514/6.2022-1809.

[11] Eberhart, C. J., West, J., and Korzun, A. M., "Overview of Plume-Surface Interaction Data from Subscale Inert Gas Testing at NASA MSFC Test Stand 300 Vacuum Facilities," *AIAA SCITECH 2022 Forum*, AIAA, 2022. https://doi.org/10.2514/6.2022-1811, URL https://arc.aiaa.org/doi/abs/10.2514/6.2022-1811.

[12] Metzger, P. T., "Rocket Exhaust Blowing Soil in Near Vacuum Conditions Is Faster than Predicted by Continuum Scaling Laws," *Earth and Space 2016*, 2016, pp. 58–66. https://doi.org/10.1061/9780784479971.007, URL https://ascelibrary.org/doi/abs/10.1061/9780784479971.007.

[13] Rasmont, N., Al-Rashdan, H. T., Elliott, G., Rovey, J., and Roca, L. V., "Millimeter Wave Interferometry for Ejecta Concentration Measurements in Plume-Surface Interactions," *AIAA SCITECH 2022 Forum*, AIAA, 2020, p. 2421. https://doi.org/10.2514/6.2022-2421, URL https://arc.aiaa.org/doi/abs/10.2514/6.2022-2421.

[14] Rasmont, N., Al-Rashdan, H., Elliott, G. S., Rovey, J., and Villafañe Roca, L., "Spatially Distributed Measurements of Ejecta Concentrations in Plume-Surface Interactions using Millimeter Wave Interferometry," *AIAA SCITECH 2023 Forum*, 2023, p. 0465.

[15] Al-Rashdan, H., "Supersonic Underexpanded Flow Visualization in Sub-Atmospheric Facility," *AIAA AVIATION 2021 FORUM*, AIAA, 2021. https://doi.org/10.2514/6.2021-2859, URL https://arc.aiaa.org/doi/abs/10.2514/6.2021-2859.

[16] Franquet, E., Perrier, V., Gibout, S., and Bruel, P., "Free underexpanded jets in a quiescent medium: A review," *Progress in Aerospace Sciences*, Vol. 77, 2015, pp. 25–53. https://doi.org/https://doi.org/10.1016/j.paerosci.2015.06.006, URL https://www.sciencedirect.com/science/article/pii/S0376042115000548.

[17] Mehta, M., Sengupta, A., Renno, N. O., Norman, J. W. V., Huseman, P. G., Gulick, D. S., and Pokora, M., "Thruster Plume Surface Interactions: Applications for Spacecraft Landings on Planetary Bodies," *AIAA Journal*, Vol. 51, No. 12, 2013, pp. 2800–2818. https://doi.org/10.2514/1.J052408, URL https://doi.org/10.2514/1.J052408.

[18] Morris, R. V., *Handbook of lunar soils*, Lyndon B. Johnson Space Center, 1983.

[19] Pike, W. T., Staufer, U., Hecht, M. H., Goetz, W., Parrat, D., Sykulska-Lawrence, H., Vijendran, S., and Madsen, M. B., "Quantification of the dry history of the Martian soil inferred from in situ microscopy," *Geophysical Research Letters*, Vol. 38, No. 24, 2011. https://doi.org/https://doi.org/10.1029/2011GL049896, URL https://agupubs.onlinelibrary.wiley.com/doi/abs/10.1029/2011GL049896.

[20] Spohn, T., Hudson, T., Witte, L., Wippermann, T., Wisniewski, L., Kedziora, B., Vrettos, C., Lorenz, R., Golombek, M., Lichtenheldt, R., Grott, M., Knollenberg, J., Krause, C., Fantinati, C., Nagihara, S., and Grygorczuk, J., "The InSight-HP3Mole on Mars: Lessons Learned from Attempts to Penetrate to Depth in the Martian Soil," *Advances in Space Research*, Vol. 69, 2022. https://doi.org/10.1016/j.asr.2022.02.009.

[21] Rasmont, N., Al-Rashdan, H. T., Elliott, G., Rovey, J. L., and ne, L. V., "Millimeter-Wave Interferometry for Opaque Particle-Laden Flows," *IEEE Transactions on Microwave Theory and Techniques*, Vol. 71, No. 11, 2023, pp. 4893–4905. https://doi.org/10.1109/TMTT.2023.3277527.

[22] Sun, H., Brigui, F., and Lesturgie, M., "Analysis and comparison of MIMO radar waveforms," *2014 International Radar Conference*, 2014, pp. 1–6. https://doi.org/10.1109/RADAR.2014.7060251.

[23] Hanson, K. M., "Tomographic reconstruction of axially symmetric objects from a single radiograph," *16th Intl Congress on High Speed Photography and Photonics*, Vol. 491, SPIE, 1985, pp. 180–187.

[24] Corti, S., "The problem of Abel inversion in the determination of plasma density from phase measurements," *Nuovo Cimento Lettere*, Vol. 29, 1980, pp. 25–32.

[25] Daun, K. J., Thomson, K. A., Liu, F., and Smallwood, G. J., "Deconvolution of axisymmetric flame properties using Tikhonov regularization," *Appl. Opt.*, Vol. 45, No. 19, 2006, pp. 4638–4646. https://doi.org/10.1364/AO.45.004638, URL https://opg.optica.org/ao/abstract.cfm?URI=ao-45-19-4638.

[26] Hickstein, D. D., Gibson, S. T., Yurchak, R., Das, D. D., and Ryazanov, M., "A direct comparison of high-speed methods for the numerical Abel transform," *Review of Scientific Instruments*, Vol. 90, No. 6, 2019.

[27] Turtle, E., Pierazzo, E., Collins, G., Osinski, G., Melosh, H., Morgan, J., and Reimold, W., "Impact structures: What does crater diameter mean," *Large meteorite impacts III*, Vol. 384, 2005, pp. 1–24.

[28] Stubbs, D. C., Silwal, L., Thurow, B. S., Hirabayashi, M., Raghav, V., and Scarborough, D. E., "Three-dimensional measurement of the crater formation during plume–surface interactions using stereo-photogrammetry," *AIAA Journal*, Vol. 60, No. 3, 2022, pp. 1316–1331.

[29] Balakrishnan, K., and Bellan, J., "Fluid density effects in supersonic jet-induced cratering in a granular bed on a planetary body having an atmosphere in the continuum regime," *Journal of Fluid Mechanics*, Vol. 915, 2021, p. A29. https://doi.org/10.1017/jfm.2021.29.

[30] Kong, H., Akakin, H. C., and Sarma, S. E., "A generalized Laplacian of Gaussian filter for blob detection and its applications," *IEEE transactions on cybernetics*, Vol. 43, No. 6, 2013, pp. 1719–1733.

[31] Gunn, S. R., "On the discrete representation of the Laplacian of Gaussian," *Pattern Recognition*, Vol. 32, No. 8, 1999, pp. 1463–1472. https://doi.org/https://doi.org/10.1016/S0031-3203(98)00163-0, URL https://www.sciencedirect.com/science/article/pii/S0031320398001630.

[32] Radke, R. J., *Dense Correspondence and Its Applications*, Cambridge University Press, 2012, p. 148–206. https://doi.org/10.1017/CBO9781139019682.005.

[33] Roberts, L., "The action of a hypersonic jet on a dust layer," Tech. rep., NASA, 1963.